Nano Research
2022, 15(6): 4799–4806

ISSN 1998-0124 CN 11-5974/O4
https://doi.org/10.1007/s12274-021-3802-4

Research Article

Low-cost high entropy alloy (HEA) for high-efficiency oxygen evolution reaction (OER)

Lalita Sharma[1,§], Nirmal Kumar Katiyar[2,3,§], Arko Parui[4,§], Rakesh Das[5], Ritesh Kumar[4], Chandra Sekhar Tiwary[5] (✉), Abhisek K. Singh[4] (✉), Aditi Halder[1] (✉), and Krishanu Biswas[2] (✉)

[1] *School of Basic Sciences, Advanced Materials Research Centre (AMRC), Indian Institute of Technology Mandi (H.P), Kamand, Mandi 175005, India*
[2] *Department of Materials Science and Engineering, Indian Institute of Technology Kanpur, Kanpur 208016, India*
[3] *School of Engineering, London South Bank University, London, SE10 AA, UK*
[4] *Materials Research Centre, Indian Institute of Science, Bangalore 560012, India*
[5] *Metallurgical and Materials Engineering, Indian Institute of Technology Kharagpur, Kharagpur 382355, India*
[§] *Lalita Sharma, Nirmal Kumar Katiyar, and Arko Parui contributed equally to this work.*

Received: 21 May 2021 / **Revised:** 13 July 2021 / **Accepted:** 3 August 2021

ABSTRACT

Oxygen evolution reaction (OER) is the key step involved both in water splitting devices and rechargeable metal-air batteries, and hence, there is an urgent need for a stable and low-cost material for efficient OER. In the present investigation, Co-Fe-Ga-Ni-Zn (CFGNZ) high entropy alloy (HEA) has been utilized as a low-cost electrocatalyst for OER. Herein, after cyclic voltammetry activation, CFGNZ-nanoparticles (NPs) are covered with oxidized surface and form high entropy (oxy) hydroxides (HEOs), exhibiting a low overpotential of 370 mV to achieve a current density of 10 mA/cm^2 with a small Tafel slope of 71 mV/dec. CFGNZ alloy has higher electrochemical stability in comparison to state-of-the art RuO_2 electrocatalyst as no degradation has been observed up to 10 h of chronoamperometry. Transmission electron microscopy (TEM) studies after 10 h of long-term chronoamperometry test showed no change in the crystal structure, which confirmed the high stability of CFGNZ. The density functional theory (DFT) based calculations show that the closeness of d(p)-band centers to the Fermi level (E_F) plays a major role in determining active sites.This work highlights the tremendous potential of CFGNZ HEA for OER, which is the primary reaction involved in water splitting.

KEYWORDS

high entropy alloy, cyclic voltammetry activation, oxygen evolution reaction, electrocatalyst, nanocrystalline catalyst

1 Introduction

Electrochemical water splitting is viewed as one of the simplest and environmentally benign approaches because of its sustainable and zero carbon emission attribute [1]. Electrocatalytic oxidation of water to O_2 faces challenges due to huge overpotential in oxygen evolution reaction (OER), which is the major roadblock for the storage of energy from renewable sources in the form of molecular fuels like H_2 or hydrocarbons [2]. Water splitting efficiency is further limited by sluggish kinetics in anodic OER, and the absence of suitable cost-effective catalytic materials. Hence, a lot of effort has been put forward for the development of the energy-efficient electrocatalysts.

Noble metal-based state of the art OER electrocatalysts, i.e., IrO_2 and RuO_2 are actively used for commercial applications [3]. However, scarcity and high cost of noble metal-based electrocatalysts restrict their use in large scale applications. Therefore, the utmost need is to develop a non-noble metal-based electrocatalysts to increase the overall efficiency of the water-splitting. Recently, a lot of efforts have been devoted to synthesize the transition metal-based alloys as well as their carbides, boride, and sulphides as an effective electrocatalyst for OER [4]. Nanocrystalline high entropy alloys (HEAs) offer a promising way of tuning their catalytic efficiency and durability by tailoring multi-element compositions [5]. Recently, HEAs have been utilized for electrochemical catalyst for CO_2 reduction, OER and hydrogen evolution reaction (HER) due to their unique properties [6]. Our previous studies have shown Ag-Au-Pt-Pd-Cu alloys having higher stability and efficiency for CO_2 reduction [7] and electro-oxidation for Formic acid [8]. Here, we proposed a nanocrystalline HEA electrocatalyst utilizing low-cost transition metals for OER, consisting of Co-Fe-Ga-Ni-Zn in equiatomic proportions; and henceforth denoted as CFGNZ alloy. The nanocrystalline CFNGZ alloy catalyst is prepared using the easily scalable casting-cum-comminution (CCC) method [9]. The OER performance, along with its stability and durability, has been tested and compared with state-of-art noble metal-based (RuO_2) electrocatalyst. In this work a novel HEA is reported as excellent OER catalyst, which is noble metal free and more active in comparison to standard IrO_2 and RuO_2 catalyst [3]. HEAs and allied materials are a hot topic in

Address correspondence to Chandra Sekhar Tiwary, Chandra.tiwary@metal.iitkgp.ac.in; Abhisek K. Singh, abhishek@iisc.ac.in; Aditi Halder, aditi@iitmandi.ac.in; Krishanu Biswas, kbiswas@iitk.ac.in

field of catalysis [10–12] and the reported HEA with current composition is new and not explored yet for catalysis. To rationalize the high activity of the CFGNZ alloy, the first-principles calculations based on density functional theory (DFT) calculations were carried out, which demonstrate the positions of d(p)-band centres of the surface atoms play the important role.

2 Experimental section

The pure metals, Co, Fe, Ni, Ga, Zn, were purchased from Alfa Aesar with 99.99% purity. KOH (assay > 85 %) was obtained from Hi-Media laboratories. Nafion (5%) solution was used as a binder in making the catalyst ink. All metals in equi-atomic proportions have been melted in a vacuum arc melting furnace and cast as an ingot by this technique. The as prepared ingot was melted in the furnace 2–3 times to ensure chemical homogeneity. Subsequently, the cast ingot was vacuum sealed in the quartz tube and homogenized at 1,000 °C for 24 h [13].The nanoparticles (NPs) of HEA have been prepared by the method of cryomilling, in which, the alloy ingot was initially cut into small pieces and subsequently milled at extremely low temperature (< 123 K) for six hours to obtain nanopowder. The liquid nitrogen (LN_2) having boiling temperature 77 K was used as coolant. The cryomill was fabricated in such a way that milled powder and liquid nitrogen never came in contact or even got mixed [13, 14]. This method is advantageous in the sense that it allows avoiding the cold welding of the metallic particles during high energy milling and the suppression of oxidation. It is primarily due to the extremely low temperature, where the cold welding is predominantly suppressed [15]. Hence, it is possible to form fine scaled alloy nanoparticles without much contaminations.

The UV–visible spectrometer (Thermo Scientific, UK) was utilized to record the surface plasmon resonance of nanocrystalline HEA. The Panalytical XPert empyrean system was used to study the crystallographic phase using X-ray (Cu Kα = 1.54046 Å). The particle size, elemental mapping, and their morphologies were investigated using a Transmission electron microscope (FEI, Titan G^2 60 operated at 300 kV). X-ray photoelectron spectroscopy (XPS) was used to know about the chemical states of the elements at the surface by using Nexsa instrument (Thermo Fisher Scientific) incorporating Al Kα as a source of X-ray. Electrochemical measurements have been performed in a standard three-electrode set-up with Metrohm, Autolab electrochemical workstation. The 5 mm glassy carbon electrode (GCE) was modified with catalyst ink utilized as a working electrode. Pt wire was used as the counter electrode, and Ag/AgCl was used as a reference electrode. All experiments have been carried out with Ag/AgCl as a reference electrode, which is converted to RHE by using Nernst equation: $E_{RHE} = E_{exp.} + 0.059pH + E^0_{Ag/AgCl}$, where $E^0_{Ag/AgCl} = 0.19$ V is the standard reduction potential of Ag/AgCl at room temperature. 1 M KOH aqueous solution with alkaline pH was used as electrolyte which was purged with inert N_2 gas prior to experiments. The catalyst ink was made by mixing 10 mg of catalyst in 500 µL of dimethyl formamide (DMF) solvent and 20 µL of Nafion solution (5%) as binder followed by sonication for 30 min. The 10 µL of catalyst ink was drop casted on the 5 mm diameter of GCE with a catalyst loading of 0.981 mg/cm^2, respectively. The catalyst loading remained constant in case of other catalysts as well. Prior to OER activity, catalyst surface was activated with the help of cyclic voltammetry (CV). CV activation scans were conducted in a potential window from 0.48 to 1.50 V vs. RHE at a scan rate of 50 mV/s. Linear scan voltammetry (LSV) was performed in the potential window from 0.90 to 2.0 V vs. RHE with a scan rate of 5 mV/s. A cyclic durability test was performed in the potential window from 1.21 to 1.56 V vs. RHE at a scan rate of 50 mV/s up to 6,000 CV cycles. The Tafel plots were plotted by taking the linear region of polarization curves, which were fitted in accordance with Butler-Volmer equation ($\eta = b\log j + a$, where j is current density, b is Tafel slope, and a is the intercept) to find out the mechanism of the reaction.

The Vienna *ab-initio* simulation (VASP 5.4.4) package [16] was utilized for performing all the first-principles-based density functional theory (DFT) calculations. For describing the interactions between electrons and ions, the all-electron projector augmented wave (PAW) pseudo potentials were utilized. The Perdew–Burke–Ernzerhof (PBE) functional of the generalized gradient approximation (GGA) was used for approximating electronic exchange and correlation effects [17]. An energy cut-off of 500 eV was used for selecting the plane waves. All the structures were optimized using a conjugate gradient scheme until the energies and components of forces reached 10^{-5} eV and 0.01 eV/Å, respectively. A vacuum of 18 Å was included along the c-direction to prevent interactions between the periodic images. The Brillouin zone was sampled by a 2 × 4 × 1 Monkhorst-Pack grid for slab calculations. The bottom two layers were frozen, and only the topmost layer was allowed to relax, out of the total three layers in the CFGNZ slab, to mimic the bulk behaviour. The randomly arranged sites of the disordered CFGNZ alloy was simulated by generating the special quasi-random structure (SQS) from the "mcsqs" utility of the Alloy Theoretic Automated Toolkit (ATAT) code [18]. Such quasi-random structures have been successful in reproducing catalytic and other properties of HEAs [7, 8, 19]. The 5 × 3 × 1 supercell of Ni (111) was taken for generating the CFGNZ alloy structure (Figs. S1(b) and S1(c) in the Electronic Supplementary Material (ESM)), containing 120 atoms, with the constituent elements—Co, Fe, Ga, Ni, and Zn, being equi-proportional (20% each) in composition.

3 Results and discussion

A schematic of nano-crystalline CFGNZ alloy preparation and OER reaction over the nanoparticle surface is depicted in the Fig. 1(a). The crystallographic phase identification of the nano-crystalline CFGNZ alloy was determined using an X-ray diffraction (XRD) pattern, and it is found to be face-centered cubic (FCC), as shown in Fig. 1(b). The average particle size of HEA NPs is 8 ± 4 nm; estimated using about 500 particles from bright-field transmission electron microscopy (TEM) images (Fig. 1(d)). It also possesses the diffraction rings corresponding to the FCC phase, as shown in Fig. 1(e). High resolution TEM (HR-TEM) image of NPs of CFGNZ is shown in Fig. 1(f) and their latticed-spacing was measured after fast Fourier transformation (FFT) processing of the image, shown in Fig. 1(g). It ($d_{(111)}$ = 0.202 nm) is marked over the image, which was also corroborated with the X-ray diffraction pattern. Figure 1(h) shows the elemental maps of a single CFGNZ alloy NP, indicating that the nanoparticles are chemically homogenous. The metallic nano-crystalline materials reveal the surface plasmon resonance (SPR) phenomena on electromagnetic radiation exposure, which appeared for CFGNZ alloy at 262 nm (Fig. 1(c)). Therefore, the prepared CFGNZ alloy is a homogeneous nano-crystalline material, suitable for the electrochemical catalyst materials.

XPS was performed for as-synthesized CFGNZ alloy without any treatment, post-CV-activation, and after 10 h of post chronoamperometry studies. XPS wide scan spectra of the as-prepared CFGNZ alloy and post CV activation displayed in Fig. S2 in the ESM showed the presence of all five elements. However, after 10 h of chronoamperometry studies, only Ga remained on the surface, and signal for other elements remained very weak. All

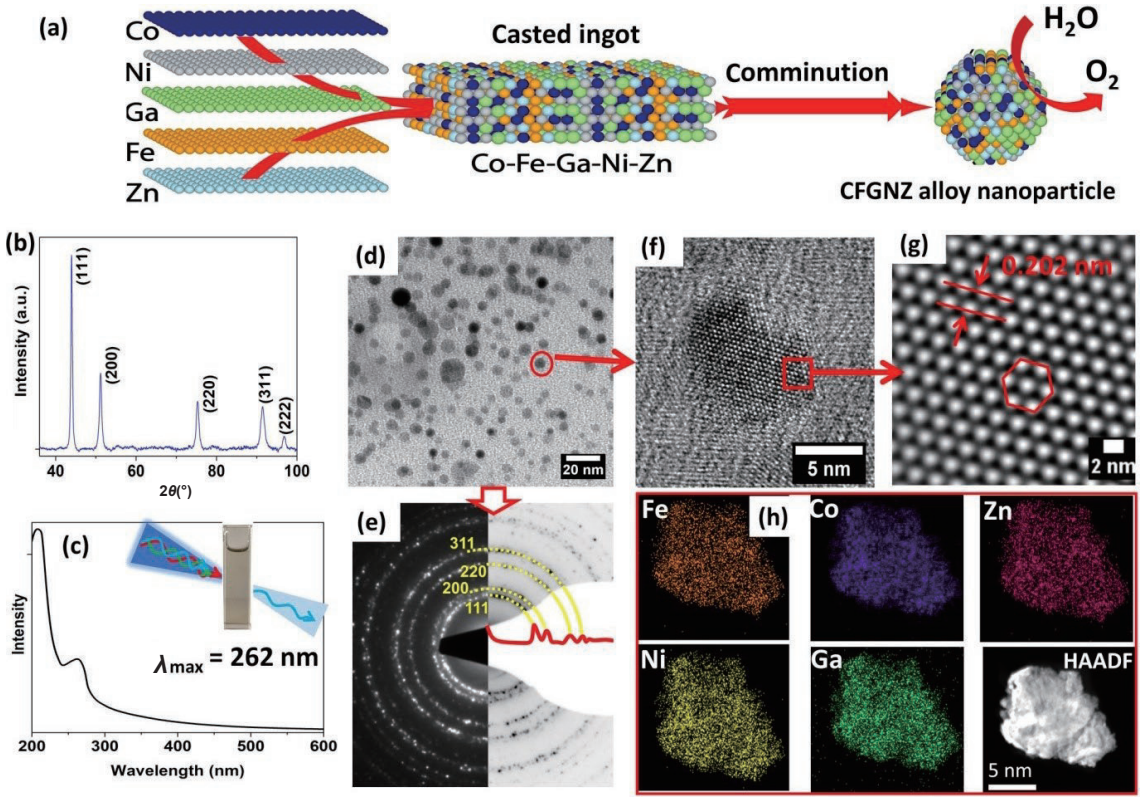

Figure 1 (a) Schematic of alloy preparation for nano-crystalline CFGNZ and catalytic reaction over its surface. (b) X-ray diffraction pattern of nano-crystalline CFGNZ alloy powder. (c) Surface plasmon resonance peak of nanoparticles (UV–visible). (d) Bright-field TEM image of CFGNZ nanoparticles and (e) corresponding ring diffraction pattern. (f) HRTEM image of single nanoparticle of CFGNZ. (g) FFT filtered image of nanoparticle corresponding to (f). (h) Elemental mapping of a single nanoparticle.

the spectra and peak fitting were carried out by taking the adventitious binding energy of C 1s at a binding energy of 284.8 eV as reference as shown in Fig. S3 in the ESM. In HEA, Ni 2p spectra confirmed the coexistence of Ni^{0+} (Ni $2p_{3/2}$, 852.2 eV; Ni $2p_{1/2}$, 870.2 eV) and Ni^{2+} on the surface as shown in Fig. 2(a). The oxidation state of the nickel at the surface of the region can be determined by the binding energies and chemical shift in the XPS spectra [20].

The peak corresponding to metallic Ni^{0+} is clearly higher than Ni^{2+} in the case of HEA, whereas after CV activation peak corresponding to Ni^{2+} is approximately equal to the metallic nickel peak, confirming the oxide formation on the surface. Enhanced intensity of Ni^{2+} peak at a binding energy of 855.6 eV after CV activation confirmed oxide formation in NiO (Ni^{2+}), which contributes to OER activities. For Fe 2p high-resolution spectra, Fe is present in metallic as well as in oxide form in the case of HEA as shown in Fig. 2(b). However, after CV activation, only the oxide form of Fe sustains, and after 10 h of chronoamperometry, iron signal becomes very weak and no traces of iron have been left at the surface, confirmed by XPS spectra. In CFGNZ alloy, the binding energies obtained at the peak position of 706.7 eV ($2p_{3/2}$) confirmed the Fe^{0+} oxidation state, whereas the absence of this peak after CV activation confirmed the complete iron oxide formation on the surface, confirmed by characteristic peaks for Fe_2O_3 [21] as Fe $2p_{1/2}$ and Fe $2p_{3/2}$ peaks at 723.4 and 710.2 eV, respectively. As shown in Fig. 2(c), the form of Co as metal is found predominantly confirmed by the peak positions at binding energies of 777.5 eV ($2p_{3/2}$) and 792.5 eV ($2p_{1/2}$), respectively. Along with metallic Co^{0+}, Co^{2+} oxidation state was also confirmed by peak positions at binding energies of 781.0 eV ($2p_{3/2}$) and 795.4 eV ($2p_{1/2}$) [22]. Along with the Co (0, +2) oxidation state, other peaks at the binding energy positions of 786.4 and 802.4 eV belong to the satellite peaks. XPS spectra of Ga in CFGNZ alloy were shown an interesting feature, as shown in Fig. 2(d). Ga 3d emission spectra were deconvoluted into two main peaks, one centred at 20.1 eV is expected of the Ga (+3) oxidation state (stoichiometric Ga_2O_3 (Ga(III)) [23]), and a second one centred at 18.0 eV corresponds to Ga(0) metallic state. Ga was present in the form of metallic as well as in the oxide forms in the case of as synthesized HEA and contributed more towards OER. One more peak in as synthesized HEA Ga 3d spectra at 23.3 eV is associated with the core level of O 2s [24]. After long term OER stability testing, Ga is the only element that remained at the surface after 10 h of stability test in both Ga(0) as well as Ga(III) oxidation state. In the case of XPS spectra of Zn, as shown in Fig. 2(e), the peaks at binding energies of 1,044.8 and 1,021.8 eV are assigned to the Zn $2p_{1/2}$ and Zn $2p_{3/2}$ peaks of Zn^{2+}, respectively [25]. After CV activation, there was no change in the oxidation state of Zn. Availability of the oxides of Ga at the top of the surface became more feasible after CV activation as a huge enhancement in the OER activities was observed due to the oxide (hydroxides). The formation of the oxides at the surface after CV activation can be further confirmed with the help of XPS spectra of O 1s in Fig. 2(f). Dual peak in O 1s XPS is indicative of the abundant surface or subsurface oxides and hydroxides as discussed in the ESM.

3.1 Electrochemical OER performance

CFGNZ alloy was activated by cyclic voltammetry prior to electrochemical testing. The surface of HEA was activated by performing CV cycles in a potential range of 0.5 to 1.6 V vs. RHE at a scan rate of 20 mV/s until stable CV curves were obtained. After completion of the 150 cycles, a stable CV curve was obtained, as shown Fig. S4 in the ESM. Subsequently, there was the formation of the more metal oxides and hydroxides at the surface confirmed by the XPS spectra of O 1s (Fig. 2(f)). After electrochemical activation, the active sites were exposed due to OH^- insertion and participated in the catalytic process. The multi metal-based (oxy) hydroxides formed at the interface of alloy assist

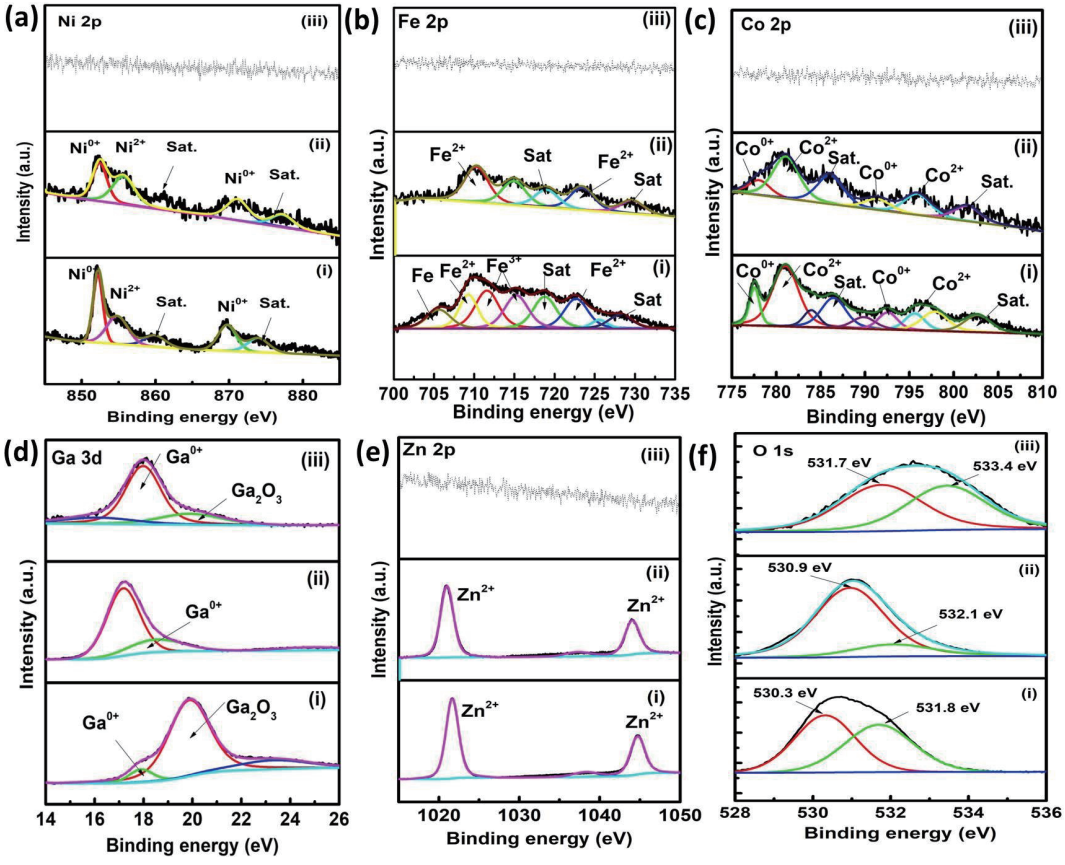

Figure 2 High resolution deconvoluted XPS spectra of (a) Ni 2p, (b) Fe 2p, (c) Co 2p, (d) Ga 3d, and (e) Zn 2p; (f) O 1s for CFGNZ alloy, after CV activation of 150 cycles and after 10 h of chronoamperometry studies in 1 M KOH electrolyte. ((i) CFGNZ alloy, (ii) after CV activation, and (iii) after 10 h of chronoamperometry testing).

the fast electron transfer, benefitting the exposure of catalytic active sites and helping to keep the morphological stability. The catalytic activity of CFGNZ (oxy) hydroxides (five element based system) exceeds in comparison to ternary (oxy) hydroxides due to the charge redistribution and optimized absorbing ability to *OH ions which play a crucial role in OER reaction [26]. OER is very sluggish process involving multiple reactions in alkaline electrolyte [27] and is expected to form HOO* as intermediate, playing a key role in oxygen evolution. (Oxy) Hydroxides formation is necessary at the surface of HEA to facilitate the formation and carry out the reaction.

$$H_2O + * \rightarrow HO^* + H^+ + e^- \quad (1)$$

$$HO^* \leftrightarrow O^* + H^+ + e^- \quad (2)$$

$$O^* + H_2O \leftrightarrow HOO^* + H^+ + e^- \quad (3)$$

$$HOO^* \leftrightarrow * + O_2 + H^+ + e^- \quad (4)$$

where * denotes the active site of HEA. As shown in Fig. 3(a), LSV curves showed the catalytic activities of HEA electrocatalyst for OER, which showed overpotential of 370 mV at a current density of 10 mA/cm^2. OER testing has also been performed for the RuO_2 state-of-the-art catalyst, which is found to be the least active in comparison to HEA. RuO_2 showed a very high overpotential of 430 mV at a current density of 10 mA/cm^2, which is 60 mV higher than HEA. In order to further elucidate the mechanism and kinetics behind the OER reaction, the Tafel slope was calculated, as shown in Fig. 3(b). A smaller slope in the plot indicates the more rapid electron transfer at the electrode/electrolyte interface at the applied potentials, suggesting the better catalytic activity of the electrocatalyst [28]. Tafel slopes for the initial HEA, RuO_2, and the HEA after 3,000 and 6,000 CV cycles are 71, 108, 63 and 63 mV/dec respectively. Tafel plot for HEA was the least as compared to state of the art catalyst RuO_2. Continuous CV cycling between 1.2 to 1.5 V vs. RHE in 1 M KOH was used to evaluate the durability, shown in Fig. S5 in the ESM. After 6,000 CV cycles, LSV curves are shown in Fig. 3(a), showing no difference in the overpotential compared to the initial HEA. The Tafel plot was also calculated after 6,000 cycles, as shown in Fig. 3(b), revealing Tafel value of 63 mV/dec, confirming no change in the overall OER performance. These results demonstrated the superior durability of the HEA in the alkaline medium. In order to evaluate the charge transfer behaviour at the interface of catalyst/electrolyte, electrochemical impedance spectroscopy (EIS) was also performed. Nyquist plot at the operating voltage of 1.5 V vs. RHE was displayed in Fig. 3(c) for RuO_2, the initial HEA, and the HEA after 3,000 and 6,000 CV cycles, respectively. Randle's equivalent circuit elements were fitted in NOVA software confirming the [R([CQ]R)] Randle's equivalent circuit, as shown in the inset of Fig. 3(c). CFGNZ forms a very small semicircle of Nyquist plot, suggesting the lower charge transfer resistance (R_{ct}) in comparison to RuO_2 and after durability testing. Whereas, semicircle in the Nyquist plot corresponds to the resistance at the CFGNZ alloy/electrolyte interface, which was tabulated in Table S2 in the ESM. CFGNZ reported very less R_{ct} of 166.9 Ω in comparison to 400.2 Ω for state-of-the-art RuO_2 electrocatalyst. EIS data is in good agreement with the LSV curves as CFGNZ alloy gives very less charge transfer resistance, consequently fast electron transfer with high OER performance. The stability of the HEA and RuO_2 electrocatalyst was evaluated by the chronoamperometry testing at a potential of 1.5 V vs. RHE for 10 h, as shown in Fig. 3(d). After completing 10 h of stability test, HEA has 80% current retention and very little material degradation. However, in the case of RuO_2,

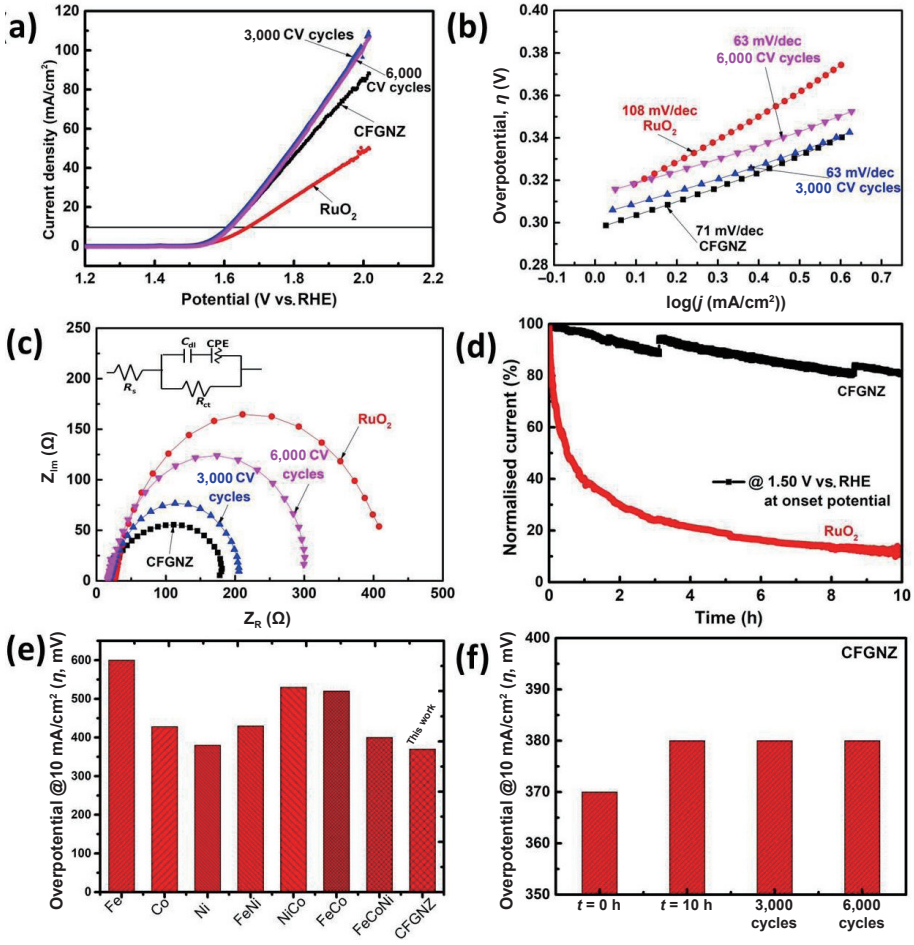

Figure 3 (a) LSV curves, (b) Tafel plot, and (c) Nyquist plot for RuO_2, the initial HEA, and the HEA after 3,000 and 6,000 CV cycles. (d) Chronoamperometry studies for RuO_2 and HEA at operating voltage of 1.5 V vs. RHE in 1 M KOH electrolyte. (e) Comparative analysis of overpotential @ 10 mA/cm² for metals, bimetallic, trimetallic and high entropy alloys obtained from reported literatures (see the ESM). (f) Overpotential at time t = 0 and 10 h and after 3,000 and 6,000 CV cycles in 1 M KOH electrolyte.

only 30% of material retained after completion of 10 h with a maximum loss of the material upto initial 4 h. The chronoamperometry test showed tremendous stability of HEA with retained OER activity even after 10 h. As shown in Fig. S6(a) in the ESM, there was almost negligible change in OER performance of HEA after 10 h of stability test. The overpotential observed at current density of 10 mA/cm² at t = 0 and after t = 10 h was 370 mV and hence, falls in the category of excellent electrocatalyst [1]. The Nyquist plot is shown in Fig. S6(b) in the ESM obtained at an operating voltage of 1.5 V after stability testing, confirming very small change in the charge transfer resistance of HEA. Furthermore, TEM was also performed to find out the changes occurred in the material after 10 h of long-term chronoamperometry test. The overpotential of high entropy alloy was compared with the other bimetallic and trimetallic alloys with the help of as reported literatures as shown in Fig. 3(e), which confirmed the least overpotential of CFGNZ alloy. Overpotential calculation at current density of 10 mA/cm² after 10 h of chronoamperometry testing was checked as shown in Fig. 3(f), which suggests the superior activity of catalyst with no appreciable change in OER performance. The sample was taken out after 10 h of chronoamperometry testing, and TEM was also performed. The nanoparticles were scratched from the electrode to carry out the post-reaction TEM analyses. At this stage, nanoparticles were not free as having an oxide layer over the surface. Subsequently, the alloy nanoparticles were characterized using TEM, as shown in Fig. 4.

The HRTEM image in Figs. 4(b) and 4(c) confirmed the oxide formation as d-spacing increases, compared to the HRTEM image of the as-prepared CFGNZ alloy. In addition, the diffraction ring pattern of nanoparticles reveals the existence of nanocrystalline materials having oxide layer. However, it does not show well-distinguished rings for different metallic oxides. The elemental maps of the NPs reveal homogeneity along with the oxygen content, as shown in Fig. 4(f). This was absent before chronoamperometry test with electrolyte. Similar results were also observed in XPS, but the XPS measurements don't reveal the existence of elements in the as-prepared alloy, rather oxides.

3.2 Theoretical studies

To gain mechanistic insights into the efficient OER reaction on the CFGNZ alloy, we also performed DFT calculations. Ni was chosen as the parent structure for generating the FCC-HEA structure with optimized lattice parameters (a = b = c = 3.52 Å, Fig. S1(a) in the ESM), which is in excellent agreement with the previous reports [29]. The (111) facet was selected for DFT calculations, as it shows the most prominent peak in the XRD pattern (Fig. 1(b)). The interlayer distance in the DFT-obtained HEA structure was found to be 2.10 Å, in good agreement with the experiments. Next, quantification of the catalytic activity (or overpotential) of OER on HEA surface was performed using the computational hydrogen electrode (CHE) model proposed by Nørskov et al. [30]. It is determined by the adsorption energies of three intermediates (*OH, *O, and *OOH) involved in the reaction [31]

$$\Delta E_{OH} = E(^*OH) - [E^* + E(H_2O) - 0.5E(H_2)] \quad (5)$$

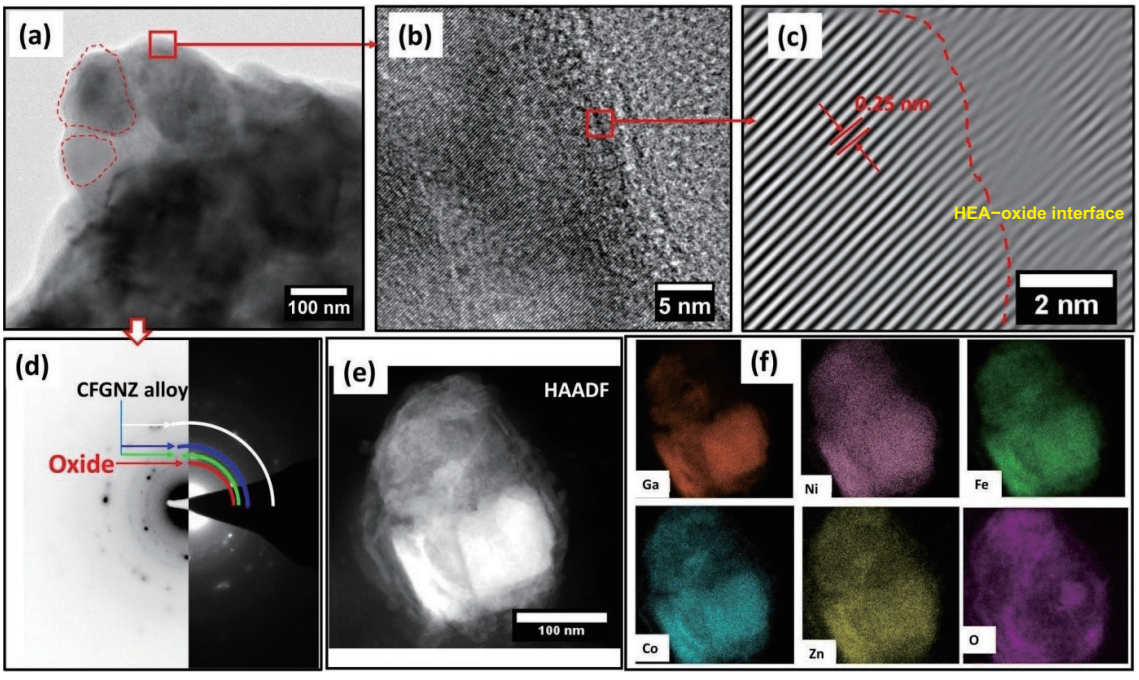

Figure 4 CFGNZ alloy NPs after 10 h of chronoamperometry testing. (a) Bright-field TEM image, (b) HRTEM image of NP, (c) FFT filtered image of (b), (d) selected area ring diffraction pattern, (e) high angle annular dark (HAADF) field image of a nanoparticles, and (f) elemental mapping of the nanoparticles.

$$\Delta E_{\mathrm{O}} = E(^{*}\mathrm{O}) - [E^{*} + E(\mathrm{H_2O}) - E(\mathrm{H_2})] \quad (6)$$

$$\Delta E_{\mathrm{OOH}} = E(^{*}\mathrm{OOH}) - [E^{*} + 2E(\mathrm{H_2O}) - 1.5E(\mathrm{H_2})] \quad (7)$$

where * represents the catalyst surface. These intermediate adsorption energies were then utilized for calculating free energies of adsorption (ΔG_{ads}) [32, 33]

$$\Delta G_{\mathrm{ads}} = \Delta E_{\mathrm{ads}} + \Delta \mathrm{ZPE} - T\Delta S + \Delta G_{\mathrm{U}} \quad (8)$$

where ΔZPE is the difference in zero-point energies of the reactants and products (Table S3 and Fig. S7 in the ESM), $T\Delta S$ is the difference in vibrational entropies (Table S3 in the ESM), and ΔG_{U} (= − eU; e is the number of electrons transferred) is the free energy corrections due to electrode potentials. The value of T was taken to be 298 K. However, in the case of CFGNZ alloy, due to the combinatorial explosion of the possibilities of catalytically active sites, the prospective sites have to be selected rationally, e.g., based on d(p)-band center ($E_{\mathrm{d(p)BC}}$) values [7, 8]. Hence, the $E_{\mathrm{d(p)BC}}$ for all the sites on the surface of the

CFGNZ alloy slab (Fig. S6(b) in the ESM) is plotted in Fig. S7 in the ESM. It is evident that $E_{\mathrm{d(p)BC}}$ of Ga, Fe, and Co sites is closer to the Fermi level (E_{F}) compared to that of Ni and Zn sites. In general, the sites with the $E_{\mathrm{d(p)BC}}$ closer to the E_{F} are more chemically active than those with the $E_{\mathrm{d(p)BC}}$ away from the E_{F} [38]. Therefore, we selected the Ga site, which has $E_{\mathrm{d(p)BC}}$ closest to the E_{F}. Experimental (chronoamperometry and CV activation) studies also suggest Ga to be the possible active sites for OER on the HEA surface. Hence, the profile for OER free energy on the HEA surface at the Ga site has been plotted in Fig. 5(a) using Eqs. (5)–(8). The free energies at 0 and 1.23 V (standard oxidation potential for water) depict that the conversion of *OH to *O intermediate is the potential determining step (PDS). The free energy corresponding to this step (ΔG_{max}) is 1.52 eV at U = 0 V, and at a potential of 1.52 V, the free energy profile becomes downhill. Therefore, theoretical overpotential (η^{the}) for OER on the CFGNZ alloy at the Ga site is given by ($\Delta G_{\mathrm{max}}/e$ − 1.23) = 0.29 V, which is closer to the experimental value (η^{exp}) of 0.37 V at a current density (j) of 10 mA/cm^2. To justify the high catalytic performance of CFGNZ alloy as compared with other state-of-the-art catalysts, we plotted their − η^{exp} at j = 10 mA/cm^2 as a function of their ΔG_{O} − Δ G_{OH} values (Fig. 5(b)) since it is the widely employed descriptor for OER at various catalyst surfaces [37]. The CFGNZ alloy lies on the top of the volcano plot, and its ΔG_{O} − Δ G_{OH} value is also optimum (neither too strong nor too weak) compared to other catalysts such as rutile oxides (strong binding) and perovskites (weak binding). Hence, following the Sabatier's principle, the CFGNZ alloy acts as a highly efficient electrocatalyst for OER. Further, it is also expected from Fig. S7 in the ESM that the alloys GaFe, GaCo, and GaFeCo may have comparable catalytic activity to that of the CFGNZ HEA for OER. However, the effect of Ni and Zn sites cannot be ignored inspite of their d-band centres being far from the Fermi level. It can be attributed to the lowering of the d-band centres of Ga, Fe, and Co sites due to the complex interplay of strain and ligand effects from all the elements present in the CFNGZ HEA. Removing the Ni and Zn atoms may not lead to optimal positioning of the d-band centres, hence it is not guaranteed that the GaFe, GaCo, and GaFeCo alloys will be active for OER.

3.3 Proposed OER mechanism for CFGNZ alloy

In an alkaline medium, the mechanism of OER is blurry as five different metal atoms are involved and the active metal centre in this scenario is quite challenging. However, theoretical studies provide a useful tool to figure out the active centre in the present case. As discussed in the earlier section, both experimental and theoretical studies provide an insight for O–O bond formation in oxygen evolution reaction in alkaline medium. Before electrochemical test, the HEA surface was activated in order to form oxides as well as hydroxides on the top of the electrode surface, shown in Fig. 5(c), responsible for the catalytic activities. As in the case of OER, the formation of oxygenated species originating from the aqueous electrolyte during activation is expected to play decisive role in determining the catalyst performance [28]. In this study, 1 M KOH was used as an aqueous electrolyte, which is rich in OH^- species coordinated to Ga to form intermediates GaOH*, GaO* and GaOOH*. Free energy calculations suggest that conversion of *OH to *O is the rate-determining step, confirmed by the theoretical studies. The OH^- species make the bond with GaO*, and there is the coupling for

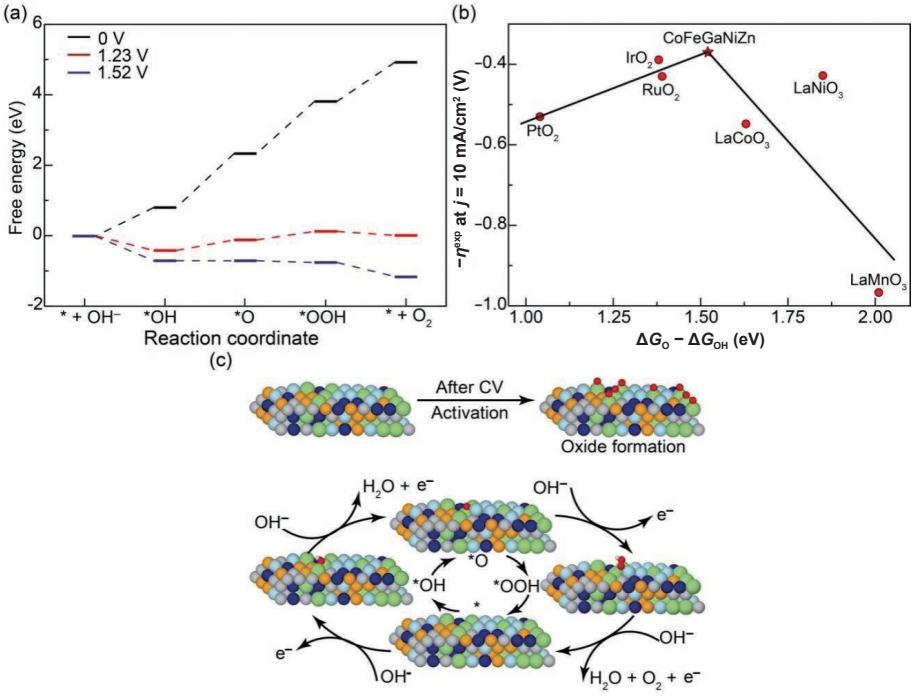

Figure 5 (a) Free energy diagram of OER on the CFGNZ alloy surface. (b) The OER volcano plot for various state-of-the-art catalysts, including the CFGNZ alloy shown against their descriptor ($\Delta G_O - \Delta G_{OH}$) values. The experimental values of overpotentials were obtained from Refs. [34–36], and the theoretical values were obtained from Ref. [37].(c) Proposed mechanism of OER at the surface of CFGNZ alloy in alkaline medium (1 M KOH; gallium—yellow balls, cobalt—blue balls, zinc—orange balls, iron—red balls, nickel—green balls, oxygen—grey balls).

the O–O bond formation, which releases in the form of O_2 leaving behind the active site of Ga free for next OH^- adsorption. In this way, HEA takes part in O_2 evolution with Ga as active centre at the interface of HEA/electrolyte. OER mechanism in the CFGNZ alloy surface will definitely help the other researchers to understand the role of the active metal centres, significantly contributing the catalytic activity.

4 Conclusions

In summary, we have proposed a cost-effective, easy scalable nanocrystalline HEA materials preparation recipe for OER study. The HEAs OER shows areduced overpotential of 370 mV at the current density of 10 mA/cm^2, as well as the Tafel slope of 71 mV/dec, respectively. It exhibits outstanding durability of up to 6,000 cycles as well as 10 h stability with no overall change in the OER performance. The theoretical DFT study further establishes the efficacy of CFGNZ alloy for OER compared to other state-of-the-art catalysts based on optimum $\Delta G_O - \Delta G_{OH}$ value. Besides, this study will strengthen the understanding of mechanism at the CFGNZ/electrolyte surface providing a new high performance of high entropy OER electrocatalyst. This will further guide to design more efficient OER catalysts in near future. These findings support the view that the multicomponent high entropy alloy containing Co, Fe, Ga, Ni, and Zn elements is an excellent OER catalyst with the formation of metallic oxide as the active component with great significance towards the stability of CFGNZ alloy.

Acknowledgements

The authors would like to thanks SERB-DST for financial support to carry out this research. We would also like to thank the Imaging centre facilities at the Indian Institute of Technology Kanpur for TEM imaging. We acknowledge Advanced Materials Research Centre (AMRC), IIT Mandi to provide the sophisticated instrumentation facilities. A. P., R. K., and A. K. S. acknowledge Materials Research Centre, Solid State and Structural Chemistry Unit, and Supercomputer Education and Research Centre for providing the computational facilities. A. P., R. K., and A. K. S. also acknowledge the support from the Institute of Eminence (IoE) MHRD grant of the Indian Institute of Science. N. K. K. acknowledges the Newton Fellowship award from the Royal Society UK (NIF\R1\191571). C. S. T. thanks MHRD STARS for funding. C. S. T. acknowledges Science and Engineering Research Board of the Department of Science and Technology, Government of India, for support through the core research grant and Ramanujan Fellowship. C. S. T. acknowledges AOARD grant no. FA2386-19-1-4039.

Electronic Supplementary Material: Supplementary material (XPS spectra of initial CFGNZ alloy along with the oxygen content, after CV activation and after 10 h of chronoamperometry and cyclic durability of CFGNZ alloy (Figs. S2–S5); OER performance and Nyquist plot after 10 h of stability test (Fig. S6); OER performance of CFGNZ alloy compared with the metals, bimetallic and trimetallic alloys (Table S1); EIS parameters (Table S2); for computational analysis, the optimized geometric structure of CFGNZ alloyslab with different orientation view (Figs. S1(a)–S1(c)); d(p)-band centre ($E_{d(p)BC}$) with each element details (Fig. S7); energetics for OER on the CFGNZ alloy (Table S3)) is available in the online version of this article at https://doi.org/10.1007/s12274-021-3802-4.

References

[1] Tahir, M.; Pan, L.; Idrees, F.; Zhang, X. W.; Wang, L.; Zou, J. J.; Wang, Z. L. Electrocatalytic oxygen evolution reaction for energy conversion and storage: A comprehensive review. *Nano Energy* **2017**, *37*, 136–157.

[2] McCrory, C. C.; Jung, S.; Peters, J. C.; Jaramillo, T. F. Benchmarking heterogeneous electrocatalysts for the oxygen evolution reaction. *J. Am. Chem. Soc.* **2013**, *135*, 16977–16987.

[3] Lee, Y.; Suntivich, J.; May, K. J.; Perry, E. E.; Shao-Horn, Y. Synthesis and activities of rutile IrO_2 and RuO_2 nanoparticles for

oxygen evolution in acid and alkaline solutions. *J. Phys. Chem. Lett.* **2012**, *3*, 399–404.
[4] Burke, M. S.; Enman, L. J.; Batchellor, A. S.; Zou, S. H.; Boettcher, S. W. Oxygen evolution reaction electrocatalysis on transition metal oxides and (oxy) hydroxides: Activity trends and design principles. *Chem. Mater.* **2015**, *27*, 7549–7558.
[5] Kumar Katiyar, N.; Biswas, K.; Yeh, J. W.; Sharma, S.; Sekhar Tiwary, C. A perspective on the catalysis using the high entropy alloys. *Nano Energy* **2021**, *88*, 106261.
[6] Amiri, A.; Shahbazian-Yassar, R. Recent progress of high-entropy materials for energy storage and conversion. *J. Mater. Chem. A* **2021**, *9*, 782–823.
[7] Nellaiappan, S.; Katiyar, N. K.; Kumar, R.; Parui, A.; Malviya, K. D.; Pradeep, K. G.; Singh, A. K.; Sharma, S.; Tiwary, C. S.; Biswas, K. High-entropy alloys as catalysts for the CO_2 and CO reduction reactions: Experimental realization. *ACS Catal.* **2020**, *10*, 3658–3663.
[8] Katiyar, N. K.; Nellaiappan, S.; Kumar, R.; Malviya, K. D.; Pradeep, K. G.; Singh, A. K.; Sharma, S.; Tiwary, C. S.; Biswas, K. Formic acid and methanol electro-oxidation and counter hydrogen production using nano high entropy catalyst. *Mater. Today Energy* **2020**, *16*, 100393.
[9] Kumar, N.; Tiwary, C. S.; Biswas, K. Preparation of nanocrystalline high-entropy alloys via cryomilling of cast ingots. *J. Mater. Sci.* **2018**, *53*, 13411–13423.
[10] Qiu, H. J.; Fang, G.; Gao, J. J.; Wen, Y. R.; Lv, J.; Li, H. L.; Xie, G. Q.; Liu, X. J.; Sun, S. H. Noble metal-free nanoporous high-entropy alloys as highly efficient electrocatalysts for oxygen evolution reaction. *ACS Mater. Lett.* **2019**, *1*, 526–533.
[11] Ding, Z. Y.; Bian, J. J.; Shuang, S.; Liu, X. D.; Hu, Y. C.; Sun, C. W.; Yang, Y. High entropy intermetallic–oxide core–shell nanostructure as superb oxygen evolution reaction catalyst. *Adv. Sustain. Syst.* **2020**, *4*, 1900105.
[12] Nandan, R.; Rekha, M. Y.; Devi, H. R.; Srivastava, C.; Nanda, K. K. High-entropy alloys for water oxidation: A new class of electrocatalysts to look out for. *Chem. Commun.* **2021**, *57*, 611–614.
[13] Katiyar, N. K.; Biswas, K.; Tiwary, C. S. Cryomilling as environmentally friendly synthesis route to prepare nanomaterials. *Int. Mater. Rev.*, in press, DOI: 10.1080/09506608.2020.1825175.
[14] Kumar, N.; Biswas, K. Fabrication of novel cryomill for synthesis of high purity metallic nanoparticles. *Rev. Sci. Instrum.* **2015**, *86*, 083903.
[15] Katiyar, N. K.; Biswas, K.; Tiwary, C. S.; Machado, L. D.; Gupta, R. K. Stabilization of a highly concentrated colloidal suspension of pristine metallic nanoparticles. *Langmuir* **2019**, *35*, 2668–2673.
[16] Kresse, G.; Hafner, J. *Ab initio* molecular dynamics for liquid metals. *Phys. Rev. B* **1993**, *47*, 558–561.
[17] Perdew, J. P.; Burke, K.; Ernzerhof, M. Generalized gradient approximation made simple. *Phys. Rev. Lett.* **1996**, *77*, 3865–3868.
[18] Zunger, A.; Wei, S. H.; Ferreira, L. G.; Bernard, J. E. Special quasirandom structures. *Phys. Rev. Lett.* **1990**, *65*, 353–356.
[19] Urs, K. M. B.; Katiyar, N. K.; Kumar, R.; Biswas, K.; Singh, A. K.; Tiwary, C. S.; Kamble, V. Multi-component (Ag–Au–Cu–Pd–Pt) alloy nanoparticle-decorated p-type 2D-molybdenum disulfide (MoS_2) for enhanced hydrogen sensing. *Nanoscale* **2020**, *12*, 11830–11841.
[20] Grosvenor, A. P.; Biesinger, M. C.; Smart, R. S. C.; McIntyre, N. S. New interpretations of XPS spectra of nickel metal and oxides. *Surf. Sci.* **2006**, *600*, 1771–1779.
[21] Fujii, T.; De Groot, F. M. F.; Sawatzky, G. A.; Voogt, F. C.; Hibma, T.; Okada, K. *In situ* XPS analysis of various iron oxide films grown by NO_2-assisted molecular-beam epitaxy. *Phys. Rev. B* **1999**, *59*, 3195–3202.
[22] Tan, B. J.; Klabunde, K. J.; Sherwood, P. M. A. XPS studies of solvated metal atom dispersed (SMAD) catalysts. Evidence for layered cobalt-manganese particles on alumina and silica. *J. Am. Chem. Soc.* **1991**, *113*, 855–861.
[23] Carli, R.; Bianchi, C. L. XPS analysis of gallium oxides. *Appl. Surf. Sci.* **1994**, *74*, 99–102.
[24] Petitmangin, A.; Gallas, B.; Hebert, C.; Perrière, J.; Binet, L.; Barboux, P.; Portier, X. Characterization of oxygen deficient gallium oxide films grown by PLD. *Appl. Surf. Sci.* **2013**, *278*, 153–157.
[25] Du, X. F.; Zhao, H. L.; Lu, Y.; Zhang, Z. J.; Kulka, A.; Świerczek, K. Synthesis of core-shell-like ZnS/C nanocomposite as improved anode material for lithium ion batteries. *Electrochim. Acta* **2017**, *228*, 100–106.
[26] Dai, W. J.; Lu, T.; Pan, Y. Novel and promising electrocatalyst for oxygen evolution reaction based on MnFeCoNi high entropy alloy. *J. Power Sources* **2019**, *430*, 104–111.
[27] Chen, D. J.; Chen, C.; Baiyee, Z. M.; Shao, Z. P.; Ciucci, F. Nonstoichiometric oxides as low-cost and highly-efficient oxygen reduction/evolution catalysts for low-temperature electrochemical devices. *Chem. Rev.* **2015**, *115*, 9869–9921.
[28] Katsounaros, I.; Cherevko, S.; Zeradjanin, A. R.; Mayrhofer, K. J. J. Oxygen electrochemistry as a cornerstone for sustainable energy conversion. *Angew. Chem., Int. Ed.* **2014**, *53*, 102–121.
[29] Lide, D. R. *CRC Handbook of Chemistry and Physics*, *Editor-in-Chief*; CRC Press: London, 2005.
[30] Nørskov, J. K.; Rossmeisl, J.; Logadottir, A.; Lindqvist, L.; Kitchin, J. R.; Bligaard, T.; Jónsson, H. Origin of the overpotential for oxygen reduction at a fuel-cell cathode. *J. Phys. Chem. B* **2004**, *108*, 17886–17892.
[31] Nandan, R.; Devi, H. R.; Kumar, R.; Singh, A. K.; Srivastava, C.; Nanda, K. K. Inner sphere electron transfer promotion on homogeneously dispersed Fe-N_x centers for energy-efficient oxygen reduction reaction. *ACS Appl. Mater. Interfaces* **2020**, *12*, 36026–36039.
[32] Kumar, R.; Das, D.; Singh, A. K. C_2N/WS_2 van der Waals type-II heterostructure as a promising water splitting photocatalyst. *J. Catal.* **2018**, *359*, 143–150.
[33] Kumar, R.; Singh, A. K. Electronic structure based intuitive design principle of single-atom catalysts for efficient electrolytic nitrogen reduction. *ChemCatChem* **2020**, *12*, 5456–5464.
[34] Bockris, J. O. M.; Otagawa, T. The electrocatalysis of oxygen evolution on perovskites. *J. Electrochem.* **1984**, *131*, 290–302.
[35] Sun, W.; Song, Y.; Gong, X. Q.; Cao, L. M.; Yang, J. An efficiently tuned d-orbital occupation of IrO_2 by doping with Cu for enhancing the oxygen evolution reaction activity. *Chem. Sci.* **2015**, *6*, 4993–4999.
[36] Matsumoto, Y.; Sato, E. Electrocatalytic properties of transition metal oxides for oxygen evolution reaction. *Mater. Chem. Phys.* **1986**, *14*, 397–426.
[37] Seh, Z. W.; Kibsgaard, J.; Dickens, C. F.; Chorkendorff, I.; Nørskov, J. K.; Jaramillo, T. F. Combining theory and experiment in electrocatalysis: Insights into materials design. *Science* **2017**, *355*, eaad4998.
[38] Nørskov, J. K.; Abild-Pedersen, F.; Studt, F.; Bligaard, T. Density functional theory in surface chemistry and catalysis. *Proc. Natl. Acad. Sci. USA* **2011**, *108*, 937–943.